Ocean Modelling 165 (2021) 101834

Contents lists available at ScienceDirect

Ocean Modelling

journal homepage: www.elsevier.com/locate/ocemod

On the formulation and implementation of the stress-free boundary condition over deformed bathymetry using a spectral-element-method-based incompressible Navier–Stokes equations solver

Theodoros Diamantopoulos [a,*], Peter J. Diamessis [a], Marek Stastna [b]

[a] School of Civil and Environmental Engineering, Cornell University, Ithaca, NY, USA
[b] Department of Applied Mathematics, University of Waterloo, Waterloo, ON, Canada

ARTICLE INFO

Keywords:
Incompressible Navier–Stokes equations
Spectral element method
Free-slip boundary condition
Curved bathymetry
Pseudo-traction
Internal solitary waves

ABSTRACT

Various strategies are proposed for enforcing stress-free boundary conditions on deformed domains using a weak-form-based discretization in a Cartesian frame of reference. Due to the irregularity of the computational domain and the particular type of boundary condition, a coupling between the Cartesian velocity components is introduced. As such, a different computational kernel is required for the numerical solution of the associated vector Helmholtz equation, as contrasted to what is used for the scalar unknowns of the equations. Three approaches are presented, aimed towards the exact or approximate implementation of zero tangential stress (traction) at the deformed boundary while ensuring a decoupling of the velocity components in the solution of the vector Helmholtz equation. Two of these strategies, those which approximate the free slip boundary condition, are applied to the propagation of an internal solitary wave (ISW) of depression over a deformed bathymetry. The spatial structure and amplitude of the resultant pseudo-traction, which is accurately predicted by a simple scaling estimate, are explored as a function of the ISW-based Reynolds number, Re. For the Re values considered, the pseudo-traction is negligible with respect to the corresponding no-slip tangential shear stress. The pseudo-traction-induced, time-integrated loss of ISW energy is found to be significantly weaker than the associated viscous dissipation in the interior water column. Although, at laboratory-scale or oceanic Re, an approximate free-slip boundary condition is found to yield negligible pseudo-traction, this might not be the case when an elevated eddy viscosity is used in this context as a surrogate for no-slip turbulent bottom boundary layer dynamics.

1. Introduction

The incompressible Navier–Stokes (INS) equations under the Boussinesq approximation are a commonly used mathematical model of choice to simulate highly non-linear, non-hydrostatic phenomena, with characteristic scales of $\mathcal{O}$(1 km) or less, in the stratified ocean (Winters et al., 2004; Winters and de la Fuente, 2012; Fringer et al., 2006; Durran, 2013). Typical examples of such geophysical flow phenomena are highly non-linear internal waves and the resulting turbulence formation within the wave core (Rivera-Rosario et al., 2020), tidally-driven stratified boundary layers over a bathymetric slope (Winters, 2015) and flows over ocean ridges (Perfect et al., 2018). Critical to the robust simulation of such phenomena is the prescription of physically relevant boundary conditions, namely over the deformed bathymetry. Intimately connected to the enforcement of such boundary conditions is the operator splitting approach used in the time-advancement of the INS equations.

In the context of such splitting schemes, the lack of a prognostic equation for the pressure, associated with a non-hydrostatic flow, in the INS equations is commonly dealt with by decoupling the pressure from the velocity field by implicitly enforcing, via a projection to a divergence-free space, the incompressibility constraint. The resulting equations are elliptic in nature both for the pressure and the viscous-diffusive terms of the velocity and density field, in the presence of stratification, respectively after the splitting/time discretization (see Eq. (5)). Specifically, using a popular velocity projection scheme (Karniadakis et al., 1991) the three elliptic equations, a pressure Poisson equation, a vector Helmholtz equation for the velocity field and a scalar Helmholtz equation for the density, have to be consecutively solved for the time-advancement of the flow field. Therefore, from

* Correspondence to: School of Civil and Environmental Engineering, 220 Hollister Hall, Cornell University, Ithaca, NY, 14853, USA.
E-mail address: td353@cornell.edu (T. Diamantopoulos).

https://doi.org/10.1016/j.ocemod.2021.101834
Received 17 February 2021; Received in revised form 26 May 2021; Accepted 16 June 2021
Available online 19 June 2021
1463-5003/

an implementation standpoint, the preferred strategy is to utilize one single computational kernel, which solves numerically the scalar elliptic equations, either Poisson or Helmholtz, for all field variables both scalars and vectors. Ideally, each of the components of the velocity field can be computed separately by treating the vector Helmholtz equation in the same way as its scalar counterpart. Nevertheless, the geometry of the computational domain and the type of boundary conditions for the velocity field, prescribed both by the physics of the problem as well as for stability of the numerical simulation, effectively dictate whether each velocity component can be solved independently or not.

For the simulation of highly non-linear, non-hydrostatic internal waves propagating over a bathymetry, a vast range of scales is present within the wave as determined by a wave-based Reynolds number of $\mathcal{O}(10^8)$ (Lien et al., 2014) defined using the water column depth and the propagation speed of the internal wave. Resolving such a very broad range of scales in its entirety is unrealistic in terms of computational cost. One path towards enabling the feasibility of these type of simulations is to bypass the resolution of the fine-scale, no-slip-driven, wave-induced bottom boundary layer (BBL), therefore facilitating the resolution of areas of interest e.g. regions of shear and convective instability within the wave (Lien et al., 2012; Boegman and Stastna, 2019). To this end, *traction* boundary conditions allow one to circumvent the resolution of the BBL by either emulating bulk BBL effects via the imposition of a predefined bottom-stress or by specifying a frictionless bottom boundary, i.e., a free-slip condition. Consequently, assuming that the no-slip-driven fine-scale BBL physics are not of interest (Boegman and Stastna, 2019; Sakai et al., 2020a,b). Any challenges linked to the under-resolution of the no slip BBL which may compromise the numerical experiment, are circumvented.

The enforcement of a traction boundary condition on a deformed boundary, as in the case of an actual oceanic bathymetry, introduces a coupling between the Cartesian velocity components through the definition of the stress tensor (Kundu and Cohen, 2008). Accordingly, the vector Helmholtz equation for the Cartesian components of the velocity field has to be solved under the constraint of the associated coupling of all the velocity components. A series of approaches may then be followed for the *exact* imposition of a stress-type boundary condition depending on the numerical method of choice. A point-wise rotation and the subsequent coupling of the Cartesian momentum equations on the deformed boundary was first introduced by Engelman et al. (1982) and is extensively used in various applications when a Galerkin-based numerical method is adopted (Behr, 2004; Ford et al., 2004; Cerquaglia et al., 2017). For discretizations based on the strong-form of the equations (Winters et al., 2000), a terrain-following coordinate system is commonly utilized. Nevertheless, a simplification of the transformed equations enabled by a strictly diagonal metric tensor, is necessary and is usually achieved by virtue of an orthogonal grid (Winters et al., 2000). While these strategies are designed to impose exactly any type of stress boundary condition on general geometries, the resulting coupling between the Cartesian velocity components leads to an increase of computational complexity. On the other hand, a series of assumptions can be made to simplify the equations and decouple the velocity field components, which give rise to a number of physical inconsistencies (Limache et al., 2007).

A potential solution for the above problems, has been introduced by Epifanio (2007) for a finite difference discretization, i.e., a strong-form-based numerical method, where a decoupled system of equations for the velocity field results through a series of conditions. More specifically, a system of equations for the boundary values of the velocity field is derived from the stress boundary condition and the impermeability of the boundary. A subsequent solve of the discretized boundary conditions is then performed in each time-step to specify the boundary values of the velocity field.

To our best understanding, there is a limited discussion in the literature in the context of the INS and the implementation of stress-free boundary conditions using a weak-form-based numerical method. In this work, the discretization of the INS equations is performed using the *hp* nodal version of the finite element method namely, the Spectral Element Method (SEM) (Patera, 1984). More specifically, the imposition of a stress-free boundary condition on a deformed boundary in two-dimensions is examined for the weak form of the INS equations under the Boussinesq approximation which leads to a decoupled vector Helmholtz equation for the velocity field.

First, by following a similar methodology as in Epifanio (2007), a series of decoupled boundary conditions are derived for each of the velocity components for the variational formulation of the viscous terms. Deviating from the approach followed in Epifanio (2007), the resulting boundary condition is imposed weakly in the form of a natural boundary condition which will effectively modify the variational formulation of the viscous terms. Therefore, the same computational kernel is used for all the elliptic equations in combination with the imposition of the stress-free boundary condition in a physically consistent way. Second, a series of assumptions which lead to a decoupled system for the velocity field and avoids the intricacies of modifying the variational formulation is investigated.

The efficacy of these various strategies is demonstrated for the propagation of an internal solitary wave (ISW) of depression over a Gaussian bump at three different values of wave-based Reynolds number. In particular, the structure and amplitude of the resultant *spuriously-induced* bottom tangential traction, i.e., pseudo-traction, and the predictive accuracy of a scaling estimate for the latter are explored. Under the assumptions of a decoupled velocity field, the pseudo-traction exerted on the fluid is compared to the wall shear stress for a no-slip boundary. Furthermore, the energy lost due to the pseudo-traction as the ISW crosses the Gaussian bump is computed and is found to constitute a negligible portion of the viscous dissipation of the flow in the water-column interior.

2. Equations of motion

The equations of motion of an incompressible fluid under the Boussinesq approximation are typically written as

$$\frac{\partial \mathbf{u}}{\partial t} = -\mathbf{u}\cdot\nabla\mathbf{u} - \frac{g}{\rho_0}\rho'\mathbf{k} - \frac{1}{\rho_0}\nabla p' + \nu\nabla^2\mathbf{u} \tag{1}$$

$$\frac{\partial \rho'}{\partial t} = -\mathbf{u}\cdot\nabla\rho' + \kappa\nabla^2\rho' \tag{2}$$

$$\nabla\cdot\mathbf{u} = 0\ . \tag{3}$$

Restricting the presentation to a two-dimensional flow field, $\mathbf{u}$ is the velocity vector field with components (u_x, u_z) in the (x, z) directions respectively, ρ_0 is the reference density, g is the gravitational acceleration and $\mathbf{k}$ is the unit vector in the upward (positive) direction. Additionally, ρ' is the density perturbation which originates from the decomposition (Kundu and Cohen, 2008)

$$\rho = \rho_0 + \bar{\rho}(z) + \rho'(x,z,t) \text{ with } \rho' \ll \bar{\rho} \ll \rho_0\ . \tag{4}$$

Here p' is the pressure perturbation-deviation from the hydrostatic pressure when $\rho' = 0$ and ν, κ are the molecular diffusivities which are assumed to be constant. Note that the representation of the viscous terms, i.e., vector Laplacian, in Eq. (1) is a direct result of incompressibility. Alternatively, the viscous terms can be expressed with respect to the deviatoric stress tensor as will be further described in Section 4.1, as such a representation is of critical importance in the context of weak-form-based numerical method, and the imposition of a stress-free bottom boundary condition, per the scope of this paper.

3. Time-discretization

The semi-discrete equations which arise from the velocity projection scheme (Karniadakis et al., 1991; Subich et al., 2013) are comprised of three fractional steps; the advective (non-linear) term, the pressure, which entails the implicit solve of a Poisson equation, and the viscous term are treated separately, in succession. Here, the viscous term is shown in detail, since it is during this step where any boundary conditions for the velocity field are imposed.

3.1. Viscous equation: Laplacian formulation

The evaluation of the velocity field at the next time-step is computed implicitly via a vector Helmholtz equation. Notice that as written in Eq. (1), the viscous term of the incompressible Navier–Stokes equations is usually expressed in the form of a vector Laplacian, under the assumption of a uniform kinematic viscosity

$$-\alpha\nabla^2\mathbf{u}+\mathbf{u}=\mathbf{f}\ . \tag{5}$$

Here $\alpha=\nu\Delta t/\gamma_0$ with γ_0 a positive non-zero coefficient which depends on the time discretization order (Karniadakis et al., 1991), Δt is the time-step and $\mathbf{f}$ the right-hand side. Note that the pressure Poisson equation (PPE) carries a very similar structure to Eq. (5), though without the second term on the left-hand-side. Hence, as indicated in the introduction, any machinery/computational kernel developed for the PPE, which is more computationally demanding, would be ideally applied to the solution of Eq. (5).

3.2. Density equation

The advection–diffusion equation for the density perturbation Eq. (2) follows the same temporal discretization. More specifically, the splitting scheme is broken down into two successive steps: a) the explicit advancement of the advective part and b) the implicit solve of the diffusive term, i.e., a scalar Helmholtz equation.

3.3. Weak form of the viscous equation: Laplacian formulation

In the subsequent sections, an emphasis is placed on the Helmholtz equation for the viscous term, Eq. (5), since at this step any stress-type boundary conditions are enforced. As required by the weak formulation, Eq. (5) is multiplied by a vector test function $\mathbf{v}\in\mathcal{V}$, with $\mathcal{V}\subset H^1(\Omega)$ an appropriate functional space (Deville et al., 2002)

$$-\alpha\int_\Omega \mathbf{v}\cdot(\nabla\cdot(\nabla\mathbf{u}))\,d\Omega+\int_\Omega\mathbf{v}\cdot\mathbf{u}d\Omega=\int_\Omega\mathbf{v}\cdot\mathbf{f}d\Omega\Rightarrow \tag{6}$$

$$\alpha\int_\Omega\nabla\mathbf{u}:(\nabla\mathbf{v})^T\,d\Omega+\int_\Omega\mathbf{v}\cdot\mathbf{u}d\Omega=\int_\Omega\mathbf{v}\cdot\mathbf{f}d\Omega+\alpha\oint_{\partial\Omega}(\mathbf{n}\cdot\nabla\mathbf{u})\cdot\mathbf{v}dS\ . \tag{7}$$

After performing an integration by parts, the boundary integral term which emerges in Eq. (7) corresponds to what is known in the finite element literature (Strang and Fix, 1973) as the natural boundary condition. Any Neumann or Robin type boundary conditions are enforced weakly via this boundary integral term. Dirichlet boundary conditions can be imposed strongly by lifting the known solution (Karniadakis and Sherwin, 2013). Subtleties in the prescription of this boundary integral term are critical in determining whether the free-slip condition is truly satisfied, since the integrand does not always correspond to the actual tangential stress. As such, in the next section, this boundary integral term is described in terms of its physical underpinnings along with its connection to the enforcement of the free-slip boundary condition.

4. The free-slip boundary condition

The correct specification of boundary shear stress requires that one revisits the definition of the viscous force. Following the parlance of Gresho and Sani (2000), the viscous force per unit area on any given boundary can be expressed as a function of the viscous component of the stress tensor $\boldsymbol{\tau}$ and the normal vector to the boundary $\mathbf{n}$ as

$$\mathbf{F}=\mathbf{n}\cdot\boldsymbol{\tau}\ . \tag{8}$$

Note that, $\boldsymbol{\tau}$ is the deviatoric stress tensor (Kundu and Cohen, 2008)

$$\boldsymbol{\tau}=2\mu\mathbf{S}\ , \tag{9}$$

where $\mathbf{S}=\frac{1}{2}\left(\nabla\mathbf{u}+(\nabla\mathbf{u})^T\right)$ is the strain rate tensor and $\mu=\rho_0\nu$, is the dynamic viscosity. The static component of the stress related to the pressure is omitted, since the calculation of the pressure is decoupled from the viscous component of the incompressible Navier–Stokes, following the time-splitting scheme described in Section 3. Although, $\mathbf{F}$ is formally a force per unit area, i.e., a stress, for the sake of compactness and further adhering to the terminology of Gresho and Sani (2000), we will refer to it as a "force", hereafter.

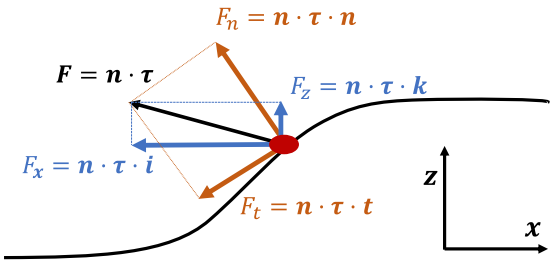

Fig. 1. A schematic of the viscous force per unit area exerted on a fluid at a deformed boundary. For a free-slip boundary condition, the tangential component of the viscous force F_t has to be zero. The viscous stress tensor $\boldsymbol{\tau}$ is responsible for coupling the velocity components. The vectors $\boldsymbol{i}$, $\boldsymbol{k}$ are the associated horizontal and vertical unit vectors and $\boldsymbol{t}$, $\boldsymbol{n}$ are the tangential and normal unit vectors on the boundary, respectively.

The viscous force on a boundary can be decomposed accordingly into its normal $F_n=\mathbf{n}\cdot\mathbf{F}$ and tangential $F_t=\mathbf{t}\cdot\mathbf{F}$ components, as schematically shown in Fig. 1. A free-slip boundary condition requires that $F_t=0$. In particular, for an *undeformed rectangular domain*, where the $\mathbf{t}$ and $\mathbf{n}$ vectors are parallel with the Cartesian axes, and for an impermeable boundary, the free-slip boundary condition is effectively imposed by simply requiring that $(\mathbf{n}\cdot\nabla\mathbf{u})_j=n_i\frac{\partial u_j}{\partial x_i}=0$. Therefore, in this particular configuration, by using the Laplacian formulation (Eq. (5)) for the viscous terms, the free-slip boundary condition can be conveniently and exactly enforced through the boundary integral term of the variational formulation in Eq. (7).

Nevertheless, for a deformed boundary, where the Cartesian velocity components do not correspond to those of the tangential and normal velocity, the free-slip boundary condition cannot be enforced as simply as in the rectangular domain case. One can easily show that $\mathbf{n}\cdot\nabla\mathbf{u}=0$ is not a sufficient condition for $F_t=0$ because

$$F_t=\mu\left(\cancelto{0}{\mathbf{n}\cdot\nabla\mathbf{u}\cdot\mathbf{t}}+\mathbf{n}\cdot(\nabla\mathbf{u})^T\cdot\mathbf{t}\right)\neq 0\ . \tag{10}$$

Consequently, if one adheres to the Laplacian formulation (Eq. (5)), the resulting natural boundary integral term in the variational formulation (Eq. (7)), used for the weak-enforcement of boundary conditions, does not necessarily correspond to the physical force (Gresho and Sani, 2000) as the second term in Eq. (10) may actually still be non-zero. Now, irrespective of the formulation of the boundary condition for the Laplacian formulation, a spurious tangential force F_p, the *pseudo-traction*, will develop at the free-slip boundary. More specifically, this pseudo-traction, for an impermeable boundary, is directly associated with the boundary's curvature namely (Kelliher, 2006)

$$F_p\approx\mu\left(\mathbf{n}\cdot(\nabla\mathbf{u})^T\cdot\mathbf{t}\right)\approx\mu\kappa(\mathbf{t}\cdot\mathbf{u})\ , \tag{11}$$

where $\kappa=\mathbf{t}\cdot\partial\mathbf{n}/\partial s$ is the curvature and s, the arc length parameterization of the boundary respectively. For a particular formulation of the free-slip condition (see Table 1), the pseudo-traction F_p may deviate from $\mu\left(\mathbf{n}\cdot(\nabla\mathbf{u})^T\cdot\mathbf{t}\right)$ since the first term of Eq. (10) may not always be set exactly to zero for all of the velocity components. Therefore, the pseudo-traction F_p scales with the dynamic viscosity μ, the tangential velocity on the boundary $\mathbf{t}\cdot\mathbf{u}$ and its curvature κ. Note that as expected, for a rectilinear boundary where $\kappa=0$, when using the Laplacian formulation the free-slip boundary condition can be imposed exactly as noted in Limache et al. (2008). In contrast, when the boundary is deformed, the homogeneous Neumann boundary conditions associated with the Laplacian formulation can be interpreted as a specific type of Navier boundary condition (Kelliher, 2006).

Table 1
Summary of the velocity boundary conditions for the different strategies of enforcing a free-slip boundary. For the IP case, the boundary conditions for each velocity component are of the homogeneous Neumann type with a subsequent velocity correction shown in Eq. (21).

Index	Type of boundary condition	Boundary condition
IF	Implicit formulation	$\mathbf{n}\cdot\nabla u_x = -\left(n_x\left(\frac{\partial\zeta}{\partial x}\right)^2 + n_z\frac{\partial\zeta}{\partial x} + 3n_x\right)\frac{\partial u_x}{\partial x} - \frac{\partial u_x}{\partial z}n_x\frac{\partial\zeta}{\partial x} - u_x\frac{\partial^2\zeta}{\partial x^2}\left(n_x\frac{\partial\zeta}{\partial x} + n_z\right)$ $u_z = u_x\frac{\partial\zeta}{\partial x}$
SA	Small angle approximation	$\mathbf{n}\cdot\nabla u_x = 0$ $u_z = u_x\frac{\partial\zeta}{\partial x}$
IP	Inviscid/pseudo-traction	$\mathbf{n}\cdot\nabla\mathbf{u} = 0$

4.1. Stress tensor formulation of the viscous equations

In light of the previous discussion, the use of a homogeneous Neumann boundary condition, as imposed through the boundary integral term of Eq. (7), in the context of prescribing a free-slip condition effectively ignores some important physics and produces a spurious viscous force at the boundary. The goal of this section is to present a variational formulation of the viscous terms in which the boundary integral term will correspond to the actual viscous force. Therefore, a traction boundary condition can be consistently enforced, introducing however some practical considerations that need to be taken into account, as discussed below.

4.1.1. The consistent natural boundary conditions

Formally, the viscous term of the INS (Eq. (1)) can be written in the more general stress-tensor-based representation

$$\frac{1}{\rho_0}\nabla\cdot\boldsymbol{\tau} = \frac{1}{\rho_0}\nabla\cdot(2\mu\mathbf{S}) = \frac{1}{\rho_0}\nabla\cdot\left(\mu\left(\nabla\mathbf{u} + (\nabla\mathbf{u})^T\right)\right) . \tag{12}$$

Notice that for an incompressible fluid the following vector identity holds

$$\nabla\cdot(\nabla\mathbf{u})^T = \nabla(\nabla\cdot\mathbf{u}) = 0 . \tag{13}$$

Therefore, for a constant viscosity μ and for a Cartesian coordinate system, the stress-tensor-based representation of the viscous term is identical to the commonly used vector Laplacian formulation of Eq. (5).

Now, the goal is to rewrite the natural boundary condition of the weak form of the viscous equation in such a way that the actual viscous force may be imposed weakly through the corresponding boundary integral term. Essential to this regard is that the viscous term in Eq. (5) be recast as a function of the stress tensor $\boldsymbol{\tau}$, shown above in Eq. (12) which leads to a modified weak form representation

$$-\beta\int_\Omega \mathbf{v}\cdot(\nabla\cdot\boldsymbol{\tau})\,d\Omega + \int_\Omega \mathbf{v}\cdot\mathbf{u}d\Omega = \int_\Omega \mathbf{v}\cdot\mathbf{f}d\Omega . \tag{14}$$

Applying integration by parts, one obtains

$$\begin{aligned}\beta\int_\Omega \boldsymbol{\tau} : (\nabla\mathbf{v})^T\,d\Omega + \int_\Omega \mathbf{v}\cdot\mathbf{u}d\Omega &= \int_\Omega \mathbf{v}\cdot\mathbf{f}d\Omega + \beta\oint_{\partial\Omega}(\mathbf{n}\cdot\boldsymbol{\tau})\cdot\mathbf{v}dS \\ &= \int_\Omega \mathbf{v}\cdot\mathbf{f}d\Omega + \beta\oint_{\partial\Omega}\mathbf{F}\cdot\mathbf{v}dS ,\end{aligned} \tag{15}$$

where $\beta = \Delta t/(\rho_0\gamma_0) = \alpha/\mu$ and $\mathbf{f} = \hat{\mathbf{u}}/\gamma_0$.

To allow a closer comparison of this modified weak form with Eq. (7), one follows the methodology of Limache et al. (2007), and substitutes Eq. (9) into Eq. (15). Eq. (14) is equivalently written as

$$\begin{aligned}\alpha\int_\Omega \nabla\mathbf{u} : (\nabla\mathbf{v})^T\,d\Omega + \int_\Omega \mathbf{v}\cdot\mathbf{u}d\Omega + \alpha\oint_{\partial\Omega}\mathbf{n}\cdot(\nabla\mathbf{u})^T\cdot\mathbf{v}dS \\ = \int_\Omega \mathbf{v}\cdot\mathbf{f}d\Omega + \beta\oint_{\partial\Omega}\mathbf{F}\cdot\mathbf{v}dS ,\end{aligned} \tag{16}$$

where it is now apparent that the boundary integral term of the left hand side causes a coupling across the equations for each velocity component (Limache et al., 2007). An immediate consequence of this integral term is that the vector Helmholtz equation now has to be solved at once for the whole velocity field. As a result, the numerical implementation of the viscous solve becomes more elaborate since additional computational complexity and memory demands need to be considered. Most importantly, the computational tool used for the numerical calculation of the scalar quantities, i.e., the density perturbation ρ' and the temporal mean of the pressure perturbation p, cannot be directly adapted for the computation of the coupled velocity components.

Now, note that although boundary integral terms are commonly used for imposing weakly a boundary condition, in this case, the integrand of the boundary term in the left hand side of Eq. (16) involves unknown quantities and cannot be prescribed *a priori*. Nonetheless, the boundary integral term in the right hand side is now the natural boundary condition, i.e., the physical viscous force exerted on the fluid and thus the physically consistent boundary condition of the Navier–Stokes equations (Gresho and Sani, 2000).

4.2. Decoupling the velocity components in the Laplacian formulation

Now that the consistent variational formulation has been defined, with its associated computational complexities, i.e., coupling of the Cartesian velocity components, it will serve as a platform for the development of a series of, either exact or approximate, approaches for the enforcement of the free-slip boundary condition in the *framework of the Laplacian formulation* of the viscous terms (Eq. (7)) which are now discussed. First, the consistent non-homogeneous Neumann boundary condition which satisfies the impermeability of the boundary, and guarantees a traction-free boundary, will be presented when the viscous terms are expressed in the form of a vector Laplacian (Eq. (7)). However, the resulting exact imposition of the free-slip boundary condition, as it will be subsequently described, leads to a more complex variational formulation which poses various questions on its numerical stability from an implementation standpoint. Two different assumptions will be then presented which, although do not guarantee an exact free-slip boundary, simplify the resulting variational formulations. Note that the common objective of these approaches for imposing the free-slip condition is to allow the independent computation of each velocity component by circumventing the coupling discussed in Section 4.1.1 .

4.2.1. Implicit formulation

The implicit formulation is constructed following the methodology of Robertson et al. (2004), for an impermeable and twice differentiable bottom boundary. The derivation of the boundary conditions for the two velocity components is discussed in more detail in Appendix A. A non-homogeneous Neumann boundary condition is derived for the horizontal velocity component u_x by rewriting the free-slip boundary condition $F_t = 0$ as

$$\begin{aligned}\mathbf{n}\cdot\nabla u_x = &-\left(n_x\left(\frac{\partial\zeta}{\partial x}\right)^2 + n_z\frac{\partial\zeta}{\partial x} + 3n_x\right)\frac{\partial u_x}{\partial x} - \frac{\partial u_x}{\partial z}n_x\frac{\partial\zeta}{\partial x} \\ &- u_x\frac{\partial^2\zeta}{\partial x^2}\left(n_x\frac{\partial\zeta}{\partial x} + n_z\right) ,\end{aligned} \tag{17}$$

where $\mathbf{n} = [n_x, n_z]$ are the components of the boundary normal vector and $\partial\zeta/\partial x$ is the boundary slope (Robertson et al., 2004). Subsequently, in the framework of the weak form of the Laplacian formulation of the viscous terms in Eq. (7), once the horizontal velocity component u_x is computed with the above boundary condition, the vertical velocity component u_z can be independently computed by enforcing the impermeability of the boundary (Eq. (18)) as a non-homogeneous Dirichlet boundary condition

$$\mathbf{n}\cdot\mathbf{u} = 0 \Rightarrow u_z = u_x\frac{\partial\zeta}{\partial x}\ . \tag{18}$$

Nonetheless, the use of the boundary condition of Eq. (17) will augment the left hand side of the weak form of the viscous operator in the form of additional boundary integral terms which may compromise the stability of the numerical method since it may constitute a "variational crime" (Brenner and Scott, 2007). The proof of stability of this more complex variational formulation is out of the scope of this study. Furthermore, from a numerical standpoint, the inclusion of terms associated with products of first or second derivatives of the bathymetry function, $\zeta(x)$, and quadratic expressions thereof, may contribute to aliasing effects even when higher-order polynomial approximations are used in the spectral-element discretization of the governing equations (Kirby and Karniadakis, 2003) along with what is apparently sufficient grid resolution of any bathymetric features at hand. This aliasing effect is particularly true in the benchmark case considered in Section 5.1 where $\zeta(x)$ is an exact Gaussian, since the representation of the bathymetry depends solely on the grid resolution. It may also be present when any in-situ sampled bathymetry is used based on lower-order, cubic-spline interpolations (Rivera-Rosario et al., 2020). Therefore in the subsequent sections, an emphasis will be given on enforcing approximately the free-slip boundary condition in a simplified variational setting, while ensuring a decoupling of the velocity components.

4.2.2. Small boundary slope approximation

The complexity in the variational formulation that is introduced via the boundary condition of Eq. (17), in the form of additional boundary integral terms, can be mitigated under the assumption of a sufficiently small boundary slope, i.e., a weak departure from the rectilinear domain, where $\partial\zeta/\partial x \approx 0$. Thus, Eq. (17) may be written as

$$\mathbf{n}\cdot\nabla u_x \approx 0\ . \tag{19}$$

Note that the impermeability of the bottom boundary needs to be satisfied exactly since it is associated with the divergence of the velocity field within the closed computational domain

$$\int_\Omega \nabla\cdot\mathbf{u}d\Omega = \oint_{\partial\Omega}\mathbf{n}\cdot\mathbf{u}dS = 0\ . \tag{20}$$

In the case where Eq. (20) is not satisfied up to machine precision, a spurious non-zero divergence may be formed which can compromise the stability of the numerical simulation. Therefore, the boundary condition for the vertical velocity component u_z is the one in Eq. (18).

4.2.3. The inviscid and pseudo-traction assumptions

Starting from the consistent viscous formulation of Eq. (16) two assumptions are made which lead to a decoupling of the velocity components. First, we assume that the viscous force exerted on the fluid at the boundary is $\mathbf{F} = \mathbf{0}$, i.e., what is regarded as an "inviscid" boundary (Limache et al., 2007). Second, the boundary integral term on the left hand side of Eq. (16) associated with the coupling of the velocity components $\mathbf{n}\cdot(\nabla\mathbf{u})^T$ and consequently the pseudo-traction F_p (Eq. (11)) is neglected. Therefore, the component of the strain rate responsible for the pseudo-traction is assumed to be zero. Thus, taking the inviscid and pseudo-traction assumptions into consideration the equation to be solved for the velocity field is identically the same as the Laplacian formulation of Eq. (7) with homogeneous Neumann boundary conditions, i.e., $\mathbf{n}\cdot\nabla\mathbf{u} = 0$ which may then also be employed in this case.

Once the velocity field is computed, a velocity correction takes place to enforce the impermeability of the boundary by projecting out the normal component of the velocity field

$$\tilde{\mathbf{u}} = \mathbf{u} - (\mathbf{n}\cdot\mathbf{u})\,\mathbf{n}\ , \tag{21}$$

where $\tilde{\mathbf{u}}$ is tangent to the bottom boundary.

5. Results

5.1. Benchmark problem configuration

The robustness of the different approaches in the enforcement of the free-slip boundary condition discussed so far is now examined through simulating the propagation of an internal solitary wave (ISW) over a Gaussian hill in a lab-scale flume with purely free-slip boundaries. In terms of the scope of the work under consideration, the particular benchmark is attractive as the ISW employed (see below) is an exact solution of the incompressible stratified Euler equations under the Boussinesq approximation (Dunphy et al., 2011). As such, it serves as a non-trivially demanding test for the accuracy and robustness of an incompressible flow solver when run in inviscid mode: in a uniform depth channel, the ISW should propagate at a constant, theoretically prescribed, speed while maintaining its initial waveform and having its total energy (sum of kinetic and available potential energy) remain unchanged. When viscous/diffusive terms are incorporated in the governing equation, in a uniform-depth free-slip channel, the ISW's propagation speed, waveform and energy content will undergo a weak adjustment due to viscous and diffusive effects in the wave interior, as determined by the values of the wave-scale Reynolds numbers (see Eq. (23)) and Schmidt numbers, $Sc = \nu/\kappa$. Neglecting the above viscous/diffusive effects, if a *gentle*, i.e., small slope, bathymetric feature, such as the Gaussian bump considered here, is now inserted the numerically simulated wave should propagate over it without any significant structural changes and should recover its original waveform a short downstream distance from the bump. Nonetheless, per Section 4 and when an approximate free-slip boundary condition is used, the finite curvature of the bump will produce a pseudo-traction which will serve as an additional form of ISW energy loss focused at the bottom boundary.

When a higher order spatial discretization is used, as is the case here, a more accurate quantification of the pseudo-traction and its impact as an energy sink is possible. On one hand, the numerical dissipation at the smallest resolved scales, in the wave interior and bottom boundary, is minimal. On the other, so is the numerical dispersion which will not spuriously interfere with any subtle physical dispersion effects of the ISW as it propagates over the bump. Furthermore, through the particular high order discretization and the isoparametric approximation of the bottom boundary via curvilinear elements (Kopriva, 2009), any spurious separation documented for analogous problems when linearly mapped elements are used (Steinmoeller et al., 2016), is not observed. Hence, any contributions to the pseudo-traction will originate from assumptions in the formulation of the approximate free-slip boundary condition.

The initial conditions of the ISW are generated via the solution of the Dubreil–Jacotin–Long (DJL) equation (Dunphy et al., 2011) for a continuous two-layer stratification given by

$$\frac{\rho}{\rho_0} = 1 - \frac{\Delta\rho}{2\rho_0}\tanh\left(\frac{z+h_1}{\delta}\right)\ , \tag{22}$$

where $\rho_0 = 1000\ \mathrm{kgm^{-3}}$ is the reference density, $\Delta\rho = 40\ \mathrm{kgm^{-3}}$ is the difference between the lower and upper densities, $h_1 = 3$ cm is the upper layer depth and $\delta = 0.5$ cm is the interface thickness. The ISW is generated for an initial available potential energy (APE) of $APE = 5\times10^{-5}\ \mathrm{m^4s^{-2}}$ with an initial wavelength $L_w \approx 0.69$ m and a

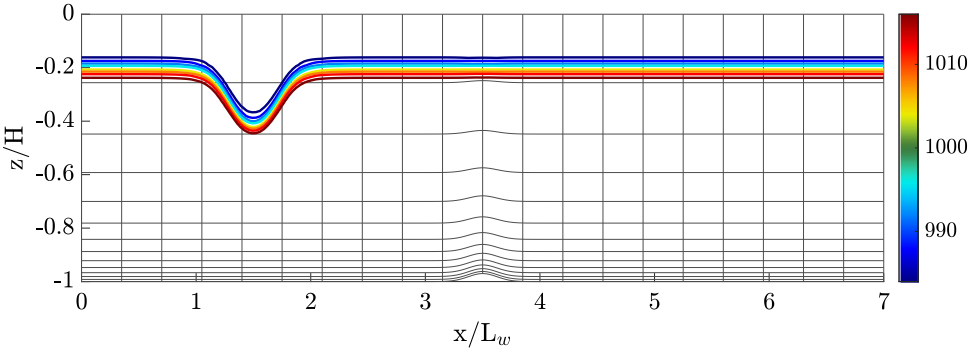

Fig. 2. The domain geometry used for the simulation of the propagation of an internal solitary wave (ISW) in a continuous two-layer stratification over a Gaussian bump. In each element, 16 × 16 Gauss–Lobatto–Legendre grid points are used. The solid coloured contour lines are the full density contours equispaced from the reference density. The rightward-propagating ISW originates at $x/L_w = 1.5$, as shown. The simulation stops once the wave trough has arrived at $x/L_w = 4$ where it has nearly recovered its original waveform, after any transient structural adjustments during the propagation of the wave over the localized bump.

propagation speed $c \approx 0.114$ ms^{-1}. The domain dimensions are, $H = 15$ cm the domain height and $L = 7 \times L_w = 4.83$ m the domain length. The centre of the Gaussian hill is placed in the middle of the computational domain with a height of $h_g = 0.03 \times H$ and width $L_g = 3 \times L_w/4$. The problem configuration is shown in Fig. 2. The simulation is stopped when the ISW arrives at a along-bed position, which is symmetric to the wave's starting position with respect to the centre of Gaussian bump.

The benchmark ISW is intentionally chosen to be moderate in amplitude, as measured by the ratio of wave-induced maximum isopycnal displacement to water column depth, which is equal to approximately 24%. Such a moderate-amplitude ISW will operate well below the convective or shear instability limits (Lamb, 2003) both in uniform depth water but also while propagating over the Gaussian bump. Such instabilities would drive elevated dissipation in the wave interior which would complicate any comparison thereof with the energy lost purely due to pseudo-traction (see Section 5.5). Finally, the choice of amplitude of Gaussian bump elevation is motivated by similar arguments, as a steeper bump would enhance the likelihood of the above flow instabilities. The maximum slope of the bump at hand is 3%, which is less than the maximum bathymetric slope found in recent observational and modelling studies of ISWs shoaling in the South China Sea (Rivera-Rosario et al., 2020; Lien et al., 2012; Lamb and Warn Varnas, 2015).

In regards to spatial discretization, the nodal version of the Spectral Element Method (SEM) (Patera, 1984) is used with $m_x = 20$ and $m_z = 13$ of quadrilateral elements in the x and z directions respectively, for a polynomial order per element per dimension $p = 15$ which corresponds to $N_x \times N_z = 301 \times 196$ grid points. The high polynomial order is chosen to minimize any numerical dissipation and dispersion, as discussed above. A grid stretching technique applied to element height is used with $\Delta z^{i-1} = 0.75 \Delta z^i$ where Δz^i is the height of the ith element.

A qualitative and quantitative assessment of the exact and approximate implementations of the free-slip boundary condition is performed for three different values of wave-based Reynolds number, Re

$$Re = cH/\nu \ . \tag{23}$$

Specifically, values of $Re = 2.5 \times 10^4$, 10^5 and 4×10^5 are chosen, with the middle value representative of an ISW propagating in a typical laboratory flume (Carr et al., 2008). Each test case is denoted as $ReXXXYY$: XXX can be 025, 100 or 400, depending on the value of Re, whereas YY can be SA and IP which correspond to the small angle approximation and inviscid/pseudo-traction approach, respectively, as elaborated in Sections 4.2.2 and 4.2.3 . An additional test case, with a no-slip bottom boundary condition is also considered, using the shorthand notation NS, at each Re to compare free-slip pseudo-traction to no-slip bottom shear stresses. For all the test-cases, the resolution along with the time-step was kept constant and dictated by the no-slip run of the highest Re number ($Re = 4 \times 10^5$) to allow comparison across different implementations and Re numbers. The time-step $dt = 6.6 \times 10^{-3}$ s, is chosen such that the initial CFL number in the vertical direction is equal to 0.33.

5.2. Tangential bottom shear stress structure

Fig. 4 shows the spatial structure of the tangential force (traction), F_t, as a function of along-bed position and time over the time interval during which ISW propagates over the Gaussian bump. The contour values of F_t are scaled by the free-stream dynamic pressure (a measure of form drag) computed based on the maximum wave-induced horizontal velocity (at the wave trough). Fig. 4 is restricted to results for $Re = 2.5 \times 10^4$: for a particular boundary condition implementation, the structure of F_t is found to be independent of Re, whereas its magnitude scales linearly with $1/Re$ as it is directly proportional to the dynamic viscosity of the fluid.

For the no-slip case, the tangential traction structure assumes values which are in direct response to bottom boundary layer formation under the wave and the resulting flow separation due to the ISW-induced adverse pressure gradient in the rear half of the wave (Boegman and Stastna, 2019). This particular structure of the tangential traction has been established prior to the arrival of the wave at the Gaussian bump and subsequently tracks the propagating wave, remaining relatively unchanged, over the Gaussian bump. Because of the moderate amplitude of the wave and steepness of the bathymetric bump, no phenomena of enhanced bottom boundary layer separation are observed, such as those reported by Harnanan et al. (2015) due to the adverse pressure gradient associated with the bathymetric bump itself. Finally, for the lowest Re considered, the magnitude of the local tangential traction can be as high as 3% of the bump-induced form drag.

In contrast, the structure of any non-zero tangential traction for the case of an approximate free-slip boundary is concentrated within a fixed region along the bottom boundary, centred around the Gaussian hill, suggesting that the geometry of the bump and, in particular, its curvature is the primary driver (Fig. 3). As such, the peak positive tangential traction develops on the top of the hill. For the lower Re considered, this peak tangential traction is no greater than 2×10^{-5} of the bump-induced form drag, a distinctly small value. The negative contour values that the tangential traction assumes for the two approximations are attributed to the overall change of sign of curvature, i.e., convex at the beginning/end of the Gaussian bump (Fig. 3). As noted in Section 4.1.1, any results of the implicit formulation are not shown due to the formation of spurious high-amplitude grid-scale oscillations in the tangential traction which may be attributed to aliasing errors. These errors result from the high order derivative terms of the bathymetry function, $\zeta(x)$ (Eq. (17)), chosen to be an exact Gaussian in our case, as well as inconsistencies potentially introduced due to the modification of the variational formulation through the boundary integral terms associated with the updated natural boundary condition for the horizontal velocity component.

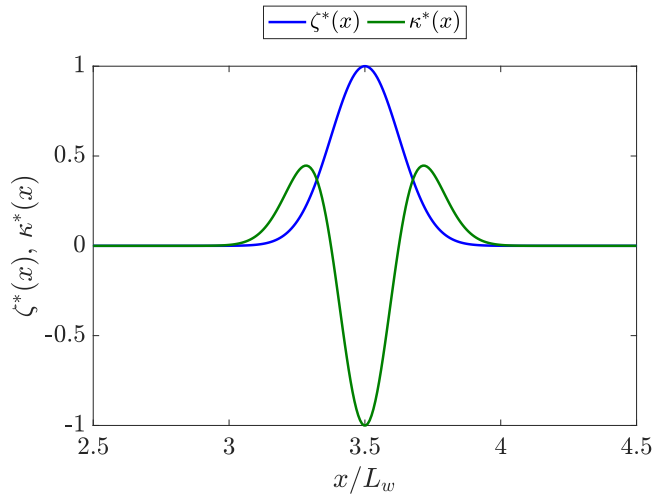

Fig. 3. Normalized bathymetric profile $\zeta^*(x)$ and curvature $\kappa^*(x)$ as a function of along-bed position.

5.3. Pseudo-traction as a function of curvature

The prediction of the pseudo-traction, per the scaling of Eq. (11), is compared to the corresponding magnitude of the tangential free-slip traction, computed from the simulation results, in Fig. 5(a)–(c). The comparison is restricted to the trough of the propagating ISW where the tangential wave-induced velocity is the largest, noting that very similar trends occur along the entire Gaussian bump. For all *Re* examined, the magnitude of the simulated tangential traction appears to scale linearly with the boundary curvature κ, with a slope very close to the theoretically predicted $\mu\,(\mathbf{t}\cdot\mathbf{u})$. Consequently, this *a priori* estimate of the pseudo-traction by virtue of its scaling, can be a useful assessment tool of the significance of the pseudo-traction based on the flow's characteristic velocity and boundary's curvature.

5.4. Free-slip to no-slip traction ratio

Fig. 4, and its higher *Re* counterparts (not shown here), indicate that the tangential traction computed from the different free-slip-implementation simulations is at least three orders of magnitude smaller than the corresponding bottom tangential stress for the no-slip case. A simple predictive scaling for the ratio of pseudo-traction F_p to no-slip traction F_w, leveraging the scaling of Eq. (11), as a function of either bump or ISW-based non-dimensional parameters is

$$\frac{F_p}{F_w} = \sqrt{\frac{H}{R}}\frac{1}{\sqrt{Re}}\,. \tag{24}$$

Details regarding the derivation are provided in Appendix B. Eq. (24) effectively indicates that the relative effect of pseudo-traction is enhanced when the radius of curvature of a bathymetric feature R is considerably smaller than the water column depth H. The practical implications of this dependence, in the context of bathymetry resolution, are further discussed in Section 6. The predicted $Re^{-1/2}$ scaling for F_p/F_w is verified for our benchmark problem simulations in Fig. 6, shown on a log–log plot since the ratio F_p/F_w follows the expected power-law behaviour (see Eq. (24)). Consistent with the scaling analysis above, the pseudo-traction and the wall shear stress are computed at the trough of the wave at the highest point of curvature of the bottom boundary, i.e., top of the Gaussian bump. Oceanically-relevant values

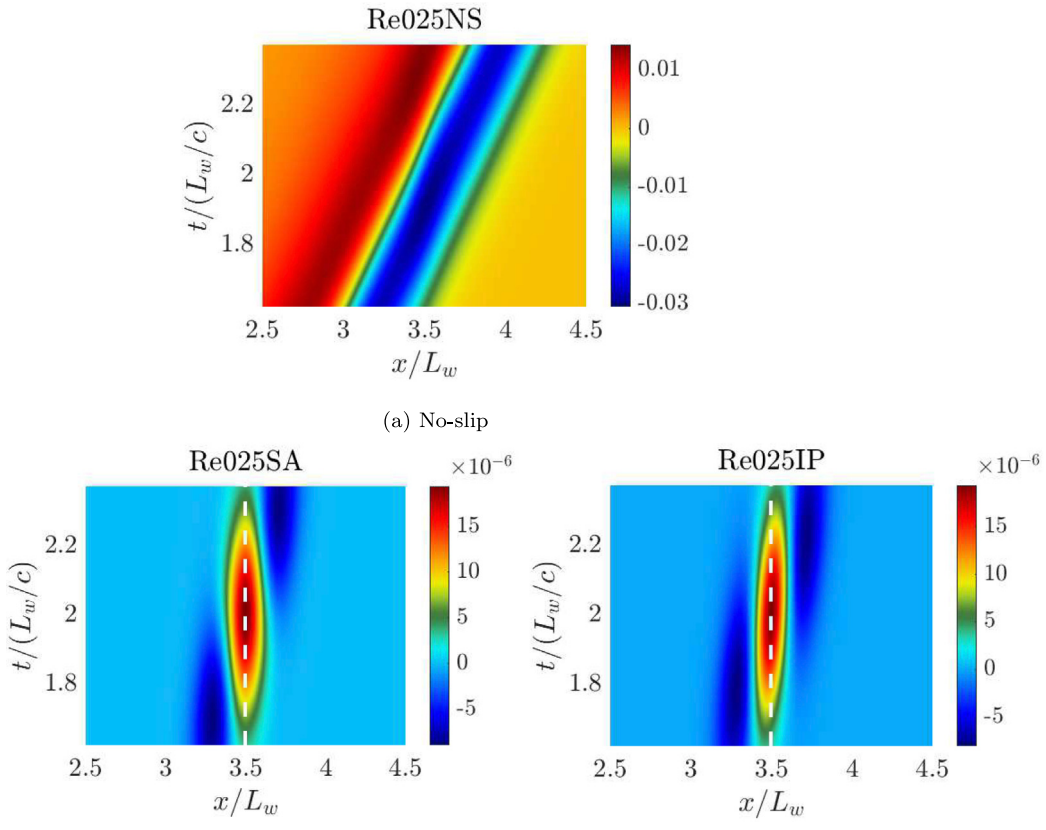

(a) No-slip

(b) Small-angle

(c) Inviscid-pseudo-traction

Fig. 4. Time evolution of the normalized tangential traction with the dynamic pressure at the trough of the wave $F_t/(\rho_0 u^2/2)$ at the bottom boundary as the ISW goes over the Gaussian hill for $Re = 2.5\times10^4$. The vertical dashed line on graphs (b & c) corresponds to the location of highest curvature.

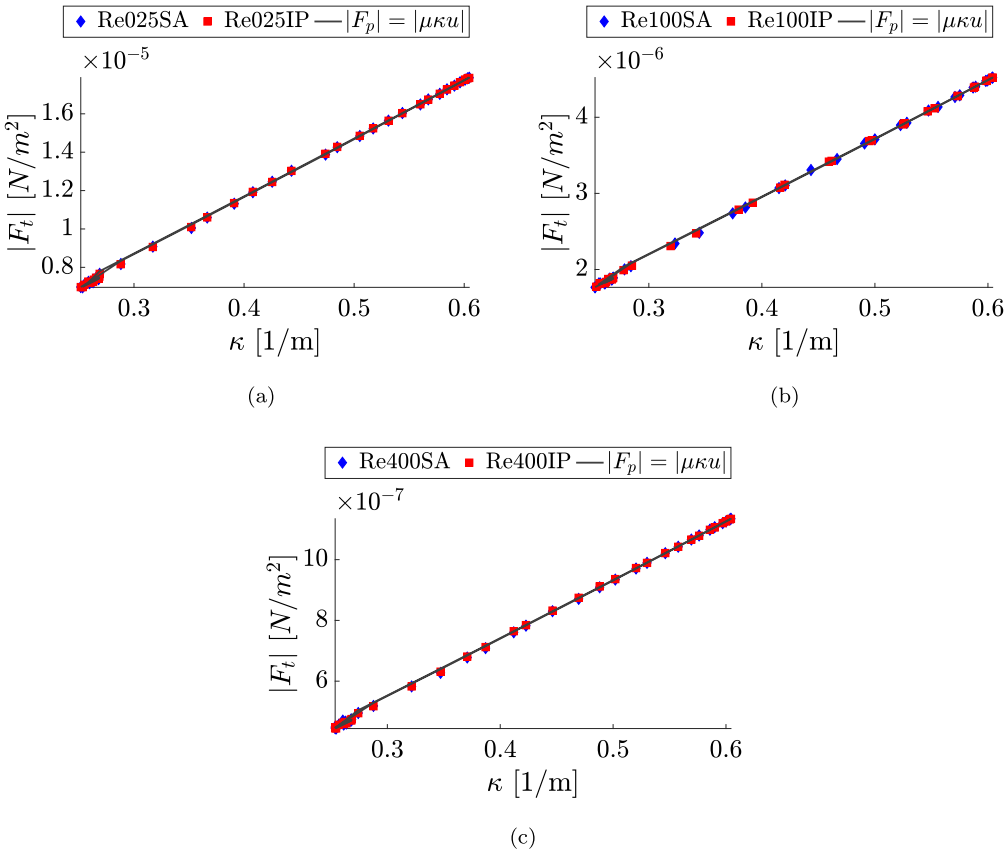

Fig. 5. (a–c) Comparison of the tangential traction F_t (data points) to the theoretical estimate of the pseudo-traction F_p (solid line) as a function of bottom boundary's curvature with respect to the three Re examined. Results are shown for locations with a curvature larger than the mean curvature of the bottom boundary. The reported tangential traction corresponds to the trough of the wave as it propagates over the Gaussian hill. The slight mismatch between the IP and SA values on panel (b) is a result of sampling the data points on different locations, to mitigate any interpolation error introduced during the computation of the ISW-induced velocity at the wave trough which does not always coincide with a grid point.

of Re can be two to three orders of magnitude larger than the ones considered here. Adhering to the potentially limiting assumptions of laminar flow and constant viscosity near the bed, pseudo-traction may be regarded practically negligible at such Re. Section 6 addresses one scenario where such a claim might need to be reconsidered.

5.5. Energy lost due to pseudo-traction

So far, we have established an understanding of the spatial structure of the free-slip-induced pseudo-traction and its dependence on bathymetric curvature, with a focus on the ISW trough which carries the maximum horizontal wave-induced velocity. We now turn to investigating the associated cumulative energy losses along the entire wave footprint and over the full time required for the ISW to propagate over the Gaussian bump. In particular, a control-volume (CV) analysis is used. The boundaries of the CV coincide with those of the computational domain. At any instance during which the ISW propagates over the bottom Gaussian bump, the rate of change of kinetic energy in the fixed CV can be calculated as (Rowe et al., 2020)

$$\frac{d\mathcal{E}}{dt} = -\oint_{\partial\Omega} \{\mathbf{u}E + p'\mathbf{u} - 2\nu\mathbf{u}\cdot\mathbf{S}\}\cdot\mathbf{n}dS + \int_{\Omega}\left(\rho' g w + 2\nu\mathbf{S}:\mathbf{S}\right)d\Omega\,, \quad (25)$$

where, $\mathcal{E}$ and $E = \rho_0\|\mathbf{u}\|^2/2$ are the total kinetic energy and kinetic energy per unit volume, respectively, $\mathbf{S}$ is the strain-rate tensor and $\mathbf{n}$ the outward wall normal vector. Notice that for impermeable boundaries $\mathbf{n}\cdot\mathbf{u} = 0$, the boundary integral of Eq. (25) is equal to

$$2\nu\oint_{\partial\Omega}\mathbf{u}\cdot\mathbf{S}\cdot\mathbf{n}dS\,, \quad (26)$$

which corresponds to the kinetic energy loss due to viscous stresses on the boundaries of the control-volume/computational-domain. Note,

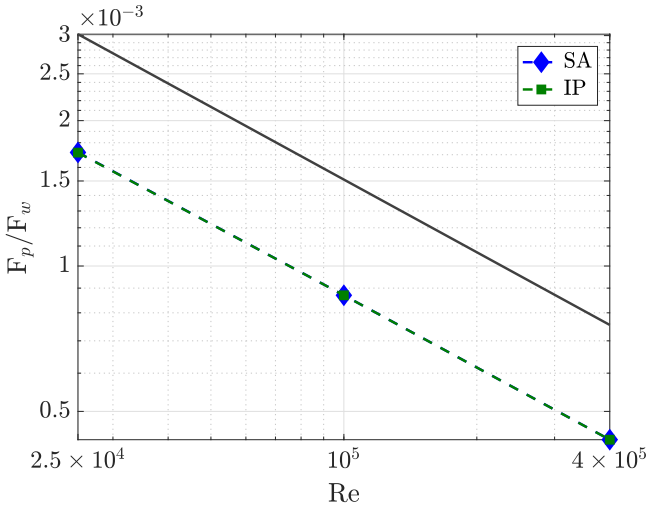

Fig. 6. Log–log plot of the ratio of the tangential traction F_t when an approximated free-slip boundary is enforced over the tangential traction for a no-slip boundary condition as a function of Re number. The solid line corresponds to a slope of $-1/2$.

that all the boundaries of the computational domain except the bottom one (Fig. 2) are non-deformed impermeable boundaries where the free-slip boundary condition is exactly enforced. Thus, any loss of kinetic energy due to physical, or spurious, viscous stresses will originate from the bottom boundary. In the case of a no-slip boundary, this integral

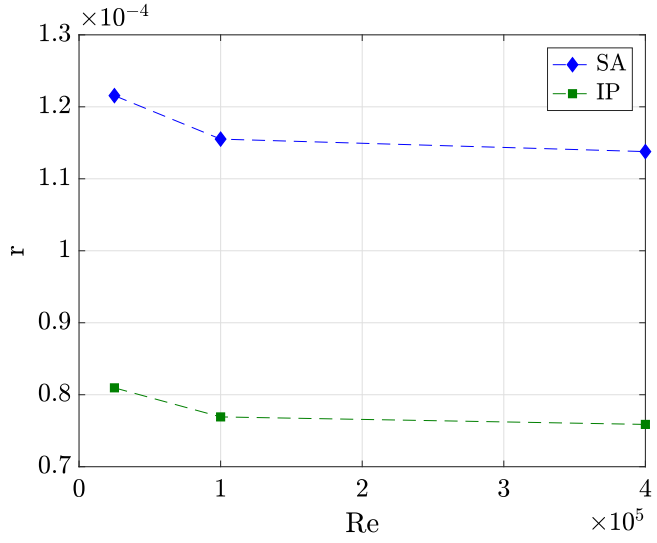

Fig. 7. Time-integrated ratio, r, of the energy lost due to viscous stresses over viscous dissipation, as a function of Re. Time-integration has been performed over the time-interval during which the ISW propagates over the Gaussian bump.

term is equal to zero since the velocity field assumes a zero value on the no-slip boundary. If, instead, an approximate free-slip boundary condition is used, pseudo-traction is expected to drive the above loss of kinetic energy. In that case, for an impermeable bottom boundary, with a tangential-only velocity component, the surface integral term (Eq. (26)), in combination with Eq. (10) becomes

$$2\nu \oint_{\partial\Omega} \mathbf{u}\cdot\mathbf{S}\cdot\mathbf{n}dS = 2\nu \oint_{\partial\Omega} u\mathbf{t}\cdot\mathbf{S}\cdot\mathbf{n}dS = \frac{1}{\rho_0}\oint_{\partial\Omega} uF_t dS\ . \tag{27}$$

One may now consider the relative importance of the time-integrated energy lost to pseudo-traction, due to the approximate enforcement of the free-slip condition, with respect to that lost due to viscous dissipation in the domain interior. In this regard, one may ignore the buoyancy flux term, i.e., the first of the two terms in the volume integral of the right-hand-side of Eq. (25). The time-integrated ratio of energy lost due to pseudo-traction and viscous dissipation may now be written as

$$r = \frac{\int_t \left(2\nu \oint_{\partial\Omega} \mathbf{u}\cdot\mathbf{S}\cdot\mathbf{n}dS\right) dt}{\int_t \left(2\nu \int_{\Omega} (\mathbf{S}:\mathbf{S})\, d\Omega\right) dt}\ . \tag{28}$$

Fig. 7 shows the dependence of r on Re for the three Reynolds numbers examined, where time-integration is applied over the time interval required for the ISW to propagate over the bottom Gaussian bump. Note the particularly small values, $O(10^{-4})$, r assumes irrespective of Re. Moreover, the ratio value r appears to asymptotically assume a constant value as Re increases and approaches its oceanic counterpart. Whereas the analysis here considers two-dimensional laminar flow in the wave interior, the presence of turbulence and elevated viscous dissipation in the wave-interior, originating from shear or convective instabilities (Lien et al., 2012, 2014; Moum et al., 2003), would reduce the value of r even further, at least in the context of a single topographic feature as considered here.

6. Discussion

The relative magnitude of the pseudo-traction on a deformed domain with respect to the equivalent bed stress of a no-slip bottom boundary, under the constraint of assuming two-dimensional laminar flow at the bottom boundary, has been examined for the benchmark of an ISW propagating over a Gaussian bump at three different Re representative of the laboratory scale or somewhat larger in value (Fig. 6). The relative magnitude of the pseudo-traction decreases with increasing Re with a $1/2$ power law as predicted by the scaling analysis of Section 5.4. Consequently, at oceanically relevant Re, of $O(10^8-10^9)$, the relative strength of the pseudo-traction is expected to be reduced by as much as a factor of 100 as compared to what is shown in Fig. 6. However, in practice, near-bed flows at such high Re will be inevitably three-dimensional and turbulent (Sakai et al., 2020a; Zulberti et al., 2020). As discussed in the introduction, a simulation of such complex three-dimensional flows is practically not feasible due to the associated high computational cost inextricably linked to the resolution required to resolve the broad range of scales, even in a partial manner. In such a case, a commonly used alternative is the use of an eddy viscosity which is often localized near the bottom (Lamb and Warn Varnas, 2015) or is set equal to a constant background value at the boundary when it changes dynamically (Klymak et al., 2010; Klymak and Legg, 2010). A commonly used value of the eddy viscosity can be up to 4 to 6 orders of magnitude larger than its molecular counterpart (Lamb and Warn Varnas, 2015; Özgökmen et al., 2004). As elaborated by Özgökmen et al. (2004), such high values will apply to both horizontal and vertical components of eddy viscosity for near-boundary flows, unlike what is the case in stratified mid-water where the vertical component can be much weaker. Therefore, when combined with the approximated free-slip boundary, use of an eddy viscosity is likely to drastically intensify the contribution of the resulting pseudo-traction to the overall flow energetics. Nevertheless, in the context of a Large Eddy Simulation (LES) subgrid scale model (Sagaut et al., 2013), additional terms related to the model, e.g., subgrid stress tensor, will be introduced in the momentum equations and thus affect the overall coupling of the velocity components. Therefore, their contribution to the overall pseudo-traction needs to be carefully studied. Nonetheless, any further investigation in the context of LES subgrid scale modelling is out of the scope of the paper.

Another possible increase of the pseudo-traction contribution, could be due to elevated curvature, i.e., reduced radius of curvature, of the bottom bathymetry (see Eq. (24)). Nevertheless, in this scenario, a practical consideration needs to be taken into account: High curvature boundaries are naturally very small in scale; accurately representing them would require very high resolution, which is prohibitive from an implementation standpoint.

Furthermore, the relative energy loss due to pseudo-traction normalized by the viscous dissipation in the domain interior is shown as a function of Re number in Fig. 7. Note, that this ratio appears to plateau as Re is increased; the energy lost due to pseudo-traction, over the time required for the wave to propagate over the Gaussian bump, is only 0.01% of the energy lost due to viscous dissipation over the same time interval. Therefore, one can safely propose, in the context of the benchmark at hand and the assumption of laminar flow within the water column, that the effect of approximating the free-slip bottom boundary condition to the overall flow energetics is also negligible in a time-integrated sense. Such a claim would hold even more strongly if highly dissipative turbulence due to shear and convective instabilities were to be present in the ISW interior, under the restriction that the near-bed flow is assumed to be laminar. However, in the case of an elevated near-bed eddy viscosity discussed above, any claim of negligible time-integrated energetic significance of pseudo-traction may have to be reconsidered.

7. Conclusions

The exact enforcement of the free-slip boundary condition on a deformed boundary introduces a coupling between the Cartesian velocity components. Consequently, solving for the velocity field under a free-slip boundary condition adds a computational complexity which can be mitigated by approximating the free-slip boundary to achieve an independent solve per each velocity component. Various free-slip approximations have been proposed for a continuous high-order Galerkin numerical discretization with a possible extension to

other weak-form-based and strong-form-based discretizations. Since the two proposed approximations are comprised of Dirichlet and Neumann type of boundary conditions, these boundary conditions can be easily enforced strongly when a strong-form-based numerical discretization is used, e.g., a finite difference method. Thus, when these approximations are adopted, the overall pseudo-traction is expected to behave in a similar manner for the same type of flow, irrespective of the numerical discretization.

The extension of these approximations to three dimensions follows naturally from its two-dimensional counterpart. Now the pseudo-traction will be a vector with two components, the tangential and binormal to the bottom boundary, with each component proportional to its respective curvature and thus to the tangent/bi-normal boundary velocity component. Therefore each component of the pseudo-traction is expected to adhere to the scaling analyses presented in Sections 4 and 5.4 .

The propagation of an internal solitary wave over a Gaussian hill has been used as a benchmark to quantify the exerted traction on the fluid due an approximate free-slip boundary condition. The tangential traction, i.e., pseudo-traction associated with the approximated free-slip boundary depends mainly on the magnitude of the tangential velocity component as well as the curvature of the deformed boundary. The energy loss attributed to the pseudo-traction compared to the total viscous dissipation, accounts to a negligible percentage, i.e., much less than 1%.

Overall, for oceanic flow modelling, the effect of the pseudo-traction seems to be negligible, alleviating the modeller from the computational intricacies of solving a coupled vector equation for the velocity field. However, the significance of the pseudo-traction to the overall flow energetics may possibly change in the case of an elevated near-bottom eddy-viscosity which poses an open question worthy of future investigation.

CRediT authorship contribution statement

Theodoros Diamantopoulos: Conceptualization, Data curation, Investigation, Methodology, Software, Visualization, Writing - original draft. **Peter J. Diamessis:** Conceptualization, Funding acquisition, Project administration, Resources, Supervision, Writing - original draft. **Marek Stastna:** Conceptualization, Writing - review & editing.

Declaration of competing interest

The authors declare that they have no known competing financial interests or personal relationships that could have appeared to influence the work reported in this paper.

Acknowledgements

The authors would like to acknowledge Professors James T. Jenkins, Luigi La Ragione, Nikolaos Bouklas and Michal Kopera for their insightful comments regarding the work in this manuscript. The authors would also like to thank the Ocean Physics and Modelling Group at the University of Athens and Professor Sarantis Sofianos for their hospitality during the final stages of writing this manuscript. Financial support is gratefully acknowledged from National Science Foundation - Division of Ocean Sciences, USA (OCE) Grant 1634257.

Appendix A. Details on the derivation of the implicit formulation

If $\mathbf{n} = [n_x, n_z]$ and $\mathbf{t} = [n_z, -n_x]$ are the components of the boundary normal and tangential vectors, (Fig. 1) and we write the velocity vector with respect to its Cartesian components $\mathbf{u} = [u_x, u_z]$, the free-slip boundary condition

$$F_t = 0 \Leftrightarrow \mu \left(\mathbf{n} \cdot \nabla \mathbf{u} \cdot \mathbf{t} + \mathbf{n} \cdot (\nabla \mathbf{u})^T \cdot \mathbf{t} \right) = 0 \,, \tag{A.1}$$

can be rewritten, following Robertson et al. (2004), as

$$\begin{aligned} n_z \left(\frac{\partial u_x}{\partial x} n_x + \frac{\partial u_x}{\partial z} n_z \right) + \frac{\partial u_z}{\partial x} n_z n_z + \frac{\partial u_x}{\partial x} n_x n_z \\ - \frac{\partial u_x}{\partial z} n_x n_x - \frac{\partial u_z}{\partial x} n_x n_x - 2 \frac{\partial u_z}{\partial z} n_z n_x = 0 \,. \end{aligned} \tag{A.2}$$

Notice that, with some rearranging and dividing through with n_z, that the first term in brackets above effectively furnishes the natural boundary condition for u_x in Eq. (6), i.e., the Laplacian formulation

$$\mathbf{n} \cdot \nabla u_x = - \frac{\partial u_x}{\partial x} n_x - \frac{\partial u_x}{\partial z} n_x \frac{\partial \zeta}{\partial x} - \frac{\partial u_z}{\partial x} \left(n_x \frac{\partial \zeta}{\partial x} + n_z \right) + 2 \frac{\partial u_z}{\partial z} n_x \,, \tag{A.3}$$

where $\zeta = \zeta(x)$ is the vertical position of the bottom deformed boundary written as a function of x and $\partial \zeta / \partial x = -n_x / n_z$ is the boundary slope as in Robertson et al. (2004). As is evident, the above boundary condition still produces a coupling between the two velocity components through the third and fourth terms in the right hand side of Eq. (A.3). Nevertheless, using the incompressibility condition

$$\nabla \cdot \mathbf{u} = \frac{\partial u_x}{\partial x} + \frac{\partial u_z}{\partial z} = 0 \Rightarrow \frac{\partial u_z}{\partial z} = - \frac{\partial u_x}{\partial x} \,, \tag{A.4}$$

and by assuming an impermeable boundary (see Eq. (18)) whose bathymetric height function is twice continuously differentiable

$$\frac{\partial u_z}{\partial x} = \frac{\partial u_x}{\partial x} \frac{\partial \zeta}{\partial x} + u_x \frac{\partial^2 \zeta}{\partial x^2} \,, \tag{A.5}$$

the natural boundary condition in Eq. (A.3) is made independent of the vertical velocity component u_z and thus, Eq. (17) is derived.

Appendix B. Scaling of pseudo-traction to bottom shear stress ratio

To this end, one focuses on the ISW trough which carries an induced horizontal current U. In the no-slip bottom case, at this location under the wave, one may assume that the development of the bottom boundary layer is driven purely by viscous diffusion and is not impacted by boundary layer separation. Under the propagating wave, the boundary layer thickness may then be approximated as $\delta \approx \sqrt{\nu t}$. If the bump's maximum radius of curvature, which occurs at its centre, is $R = 1/\kappa$, the time it takes for the wave to propagate up to this location is approximately $t \approx R/c$. Consequently, if one further assumes that the near-bed velocity profile is close to linear over a distance δ, the wall shear stress for the no-slip boundary for a purely tangential velocity $\mathbf{u} = u\mathbf{t}$, can be approximated as

$$F_w = \mu \frac{\partial u \mathbf{t}}{\partial \mathbf{n}} \approx \mu \frac{U}{\delta} = \mu U \kappa \sqrt{\frac{Rc}{\nu}} = F_p \sqrt{\frac{Rc}{\nu}} \,, \tag{B.1}$$

where $F_p = \mu U \kappa$ is the pseudo-traction due to an approximated free-slip boundary, per Eq. (11). The ratio of the pseudo-traction to the bottom shear stress may then be written as a function of the ISW-based Reynolds number as in Eq. (24).

References

Behr, M., 2004. On the application of slip boundary condition on curved boundaries. Internat. J. Numer. Methods Fluids 45 (1), 43–51.

Boegman, L., Stastna, M., 2019. Sediment resuspension and transport by internal solitary waves. Annu. Rev. Fluid Mech. 51, 129–154.

Brenner, S., Scott, R., 2007. The Mathematical Theory of Finite Element Methods, Vol. 15. Springer Science & Business Media.

Carr, M., Fructus, D., Grue, J., Jensen, A., Davies, P.A., 2008. Convectively induced shear instability in large amplitude internal solitary waves. Phys. Fluids 20 (12), 126601.

Cerquaglia, M.L., Deliége, G., Boman, R., Terrapon, V., Ponthot, J.-P., 2017. Free-slip boundary conditions for simulating free-surface incompressible flows through the particle finite element method. Internat. J. Numer. Methods Engrg. 110 (10), 921–946.

Deville, M.O., Fischer, P.F., Mund, E., et al., 2002. High-Order Methods for Incompressible Fluid Flow, Vol. 9. Cambridge University Press.

Dunphy, M., Subich, C., Stastna, M., 2011. Spectral methods for internal waves: indistinguishable density profiles and double-humped solitary waves. Nonlinear Process. Geophys. 18 (3), 351.

Durran, D.R., 2013. Numerical Methods for Wave Equations in Geophysical Fluid Dynamics, Vol. 32. Springer Science & Business Media.
Engelman, M., Sani, R., Gresho, P., 1982. The implementation of normal and/or tangential boundary conditions in finite element codes for incompressible fluid flow. Internat. J. Numer. Methods Fluids 2 (3), 225–238.
Epifanio, C.C., 2007. A method for imposing surface stress and heat flux conditions in finite-difference models with steep terrain. Mon. Weather Rev. 135 (3), 906–917.
Ford, R., Pain, C., Piggott, M., Goddard, A., De Oliveira, C., Umpleby, A., 2004. A nonhydrostatic finite-element model for three-dimensional stratified oceanic flows. Part I: Model formulation. Mon. Weather Rev. 132 (12), 2816–2831.
Fringer, O., Gerritsen, M., Street, R., 2006. An unstructured-grid, finite-volume, nonhydrostatic, parallel coastal ocean simulator. Ocean Model. 14 (3–4), 139–173.
Gresho, P., Sani, R., 2000. Incompressible Flow and the Finite Element Method, Volume 2, Isothermal Laminar Flow. Wiley.
Harnanan, S., Soontiens, N., Stastna, M., 2015. Internal wave boundary layer interaction: A novel instability over broad topography. Phys. Fluids 27 (1), 016605.
Karniadakis, G.E., Israeli, M., Orszag, S.A., 1991. High-order splitting methods for the incompressible Navier-Stokes equations. J. Comput. Phys. 97 (2), 414–443.
Karniadakis, G., Sherwin, S., 2013. Spectral/Hp Element Methods for Computational Fluid Dynamics. Oxford University Press.
Kelliher, J.P., 2006. Navier–Stokes Equations with Navier boundary conditions for a bounded domain in the plane. SIAM J. Math. Anal. 38 (1), 210–232.
Kirby, R., Karniadakis, G., 2003. De-aliasing on non-uniform grids: algorithms and applications. J. Comput. Phys. 191 (1), 249–264.
Klymak, J.M., Legg, S.M., 2010. A simple mixing scheme for models that resolve breaking internal waves. Ocean Model. 33 (3–4), 224–234.
Klymak, J.M., Legg, S.M., Pinkel, R., 2010. High-mode stationary waves in stratified flow over large obstacles. J. Fluid Mech. 644, 321.
Kopriva, D.A., 2009. Implementing Spectral Methods for Partial Differential Equations: Algorithms for Scientists and Engineers. Springer Science & Business Media.
Kundu, P., Cohen, I., 2008. Fluid Mechanics, fourth ed. Elsevier Academic Press.
Lamb, K.G., 2003. Shoaling solitary internal waves: on a criterion for the formation of waves with trapped cores. J. Fluid Mech. 478, 81.
Lamb, K., Warn Varnas, A., 2015. Two-dimensional numerical simulations of shoaling internal solitary waves at the ASIAEX site in the South China Sea. Nonlinear Process. Geophys. 22 (3).
Lien, R.-C., D'Asaro, E.A., Henyey, F., Chang, M.-H., Tang, T.-Y., Yang, Y.-J., 2012. Trapped core formation within a shoaling nonlinear internal wave. J. Phys. Oceanogr. 42 (4), 511–525.
Lien, R.-C., Henyey, F., Ma, B., Yang, Y.J., 2014. Large-amplitude internal solitary waves observed in the northern South China Sea: properties and energetics. J. Phys. Oceanogr. 44 (4), 1095–1115.
Limache, A., Idelsohn, S., Rossi, R., Oñate, E., 2007. The violation of objectivity in Laplace formulations of the Navier–Stokes equations. Internat. J. Numer. Methods Fluids 54 (6–8), 639–664.
Limache, A.C., Sánchez, P.J., Dalcín, L.D., Idelsohn, S.R., 2008. Objectivity tests for Navier–Stokes simulations: The revealing of non-physical solutions produced by Laplace formulations. Comput. Methods Appl. Mech. Engrg. 197 (49–50), 4180–4192.
Moum, J., Farmer, D., Smyth, W., Armi, L., Vagle, S., 2003. Structure and generation of turbulence at interfaces strained by internal solitary waves propagating shoreward over the continental shelf. J. Phys. Oceanogr. 33 (10), 2093–2112.
Özgökmen, T.M., Fischer, P.F., Duan, J., Iliescu, T., 2004. Entrainment in bottom gravity currents over complex topography from three-dimensional nonhydrostatic simulations. Geophys. Res. Lett. 31 (13).
Patera, A.T., 1984. A spectral element method for fluid dynamics: laminar flow in a channel expansion. J. Comput. Phys. 54 (3), 468–488.
Perfect, B., Kumar, N., Riley, J., 2018. Vortex structures in the wake of an idealized seamount in rotating, stratified flow. Geophys. Res. Lett. 45 (17), 9098–9105.
Rivera-Rosario, G., Diamessis, P.J., Lien, R.-C., Lamb, K.G., Thomsen, G.N., 2020. Formation of recirculating cores in convectively breaking internal solitary waves of depression shoaling over gentle slopes in the South China Sea. J. Phys. Oceanogr. 50 (5), 1137–1157.
Robertson, I., Sherwin, S., Graham, J., 2004. Comparison of wall boundary conditions for numerical viscous free surface flow simulation. J. Fluids Struct. 19 (4), 525–542.
Rowe, K., Diamessis, P., Zhou, Q., 2020. Internal gravity wave radiation from a stratified turbulent wake. J. Fluid Mech. 888.
Sagaut, P., Terracol, M., Deck, S., 2013. Multiscale and Multiresolution Approaches in Turbulence-LES, DES and Hybrid RANS/LES Methods: Applications and Guidelines. World Scientific.
Sakai, T., Diamessis, P.J., Jacobs, G.B., 2020a. Self-sustained instability, transition, and turbulence induced by a long separation bubble in the footprint of an internal solitary wave. I. Flow topology. Phys. Rev. Fluids 5 (10), 103801.
Sakai, T., Diamessis, P.J., Jacobs, G.B., 2020b. Self-sustained instability, transition, and turbulence induced by a long separation bubble in the footprint of an internal solitary wave. II. Flow statistics. Phys. Rev. Fluids 5 (10), 103802.
Steinmoeller, D., Stastna, M., Lamb, K., 2016. Discontinuous Galerkin methods for dispersive shallow water models in closed basins: Spurious eddies and their removal using curved boundary methods. Ocean Model. 107, 112–124.
Strang, G., Fix, G.J., 1973. An Analysis of the Finite Element Method, Vol. 212. Prentice-Hall Englewood Cliffs, NJ.
Subich, C.J., Lamb, K.G., Stastna, M., 2013. Simulation of the Navier–Stokes equations in three dimensions with a spectral collocation method. Internat. J. Numer. Methods Fluids 73 (2), 103–129.
Winters, K., 2015. Tidally driven mixing and dissipation in the stratified boundary layer above steep submarine topography. Geophys. Res. Lett. 42 (17), 7123–7130.
Winters, K.B., de la Fuente, A., 2012. Modelling rotating stratified flows at laboratory-scale using spectrally-based DNS. Ocean Model. 49, 47–59.
Winters, K., MacKinnon, J., Mills, B., 2004. A spectral model for process studies of rotating, density-stratified flows. J. Atmos. Ocean. Technol. 21 (1), 69–94.
Winters, K.B., Seim, H.E., Finnigan, T.D., 2000. Simulation of non-hydrostatic, density-stratified flow in irregular domains. Internat. J. Numer. Methods Fluids 32 (3), 263–284.
Zulberti, A., Jones, N., Ivey, G., 2020. Observations of enhanced sediment transport by nonlinear internal waves. Geophys. Res. Lett. 47 (19), e2020GL088499.